ANNUAL REVIEWS

Annual Review of Materials Research

High-Entropy Ultra-High-Temperature Borides and Carbides: A New Class of Materials for Extreme Environments

Lun Feng,[1] William G. Fahrenholtz,[1,2] and Donald W. Brenner[3]

[1]Materials Research Center, Missouri University of Science and Technology, Rolla, Missouri 65409-1170, USA; email: fenglu@mst.edu

[2]Department of Materials Science and Engineering, Missouri University of Science and Technology, Rolla, Missouri 65409-1170, USA; email: billf@mst.edu

[3]Department of Materials Science and Engineering, North Carolina State University, Raleigh, North Carolina 27695-7907, USA; email: brenner@ncsu.edu

Annu. Rev. Mater. Res. 2021. 51:165–85

First published as a Review in Advance on April 23, 2021

The *Annual Review of Materials Research* is online at matsci.annualreviews.org

https://doi.org/10.1146/annurev-matsci-080819-121217

Keywords

high-entropy ceramics, ultra-high-temperature ceramics, entropy stabilization, high-entropy borides, high-entropy carbides

Abstract

Herein, we critically evaluate computational and experimental studies in the emerging field of high-entropy ultra-high-temperature ceramics. High-entropy ultra-high-temperature ceramics are candidates for use in extreme environments that include temperatures over 2,000°C, heat fluxes of hundreds of watts per square centimeter, or irradiation from neutrons with energies of several megaelectron volts. Computational studies have been used to predict the ability to synthesize stable high-entropy materials as well as the resulting properties but face challenges such as the number and complexity of unique bonding environments that are possible for these compositionally complex compounds. Experimental studies have synthesized and densified a large number of different high-entropy borides and carbides, but no systematic studies of composition-structure-property relationships have been completed. Overall, this emerging field presents a number of exciting research challenges and numerous opportunities for future studies.

1. INTRODUCTION

Desired future capabilities related to hypersonic flight, rocket propulsion, nuclear fusion, concentrated solar power, and lightweight armor provide strong motivation in the ongoing search for new materials. Such applications involve extreme environments with combinations of temperatures, heat fluxes, chemical reactivities, radiation fluxes, strain rates, etc., that are beyond the capabilities of available materials. Ultra-high-temperature ceramics (UHTCs) have received considerable attention for their potential use in extreme environments based on properties including melting temperatures above 3,000°C, strength retention above 2,000°C, thermal conductivities of 100 W/(m·K) or higher, and thermochemical stability (1, 2). Research on UHTCs was conducted in the United States and the Soviet Union starting in the late 1950s during the space race, but few studies examined those materials in subsequent decades (3). In the 1990s, interest in hypersonic aviation led to renewed interest in UHTCs, which has continued to grow.

High-entropy materials and the entropy stabilization effect were first studied in metallic alloys consisting of five or more metals in equimolar proportions (4, 5). This concept was a paradigm shift away from alloys that consisted of a dominant element with minor amounts of additives to modify properties toward materials composed of multiple principal elements. In metallic systems, high-entropy alloys typically have the same simple crystal structures as base metals (e.g., face-centered cubic or body-centered cubic) but have improved properties including higher wear resistance, lower creep rates, and improved corrosion resistance compared to conventional alloys (6). More relevant to the present topic, refractory high-entropy alloys appear to increase the possible service temperature and improve strength compared to conventional superalloys (7). The entropy effect can drive dissolution of species into crystal structures that are not typically stable, but the effect is not strong enough to overcome the driving force for compound formation for systems in which that occurs (8).

Rost et al. (9) were the first to apply the high-entropy/entropy stabilization concept to ceramics. They demonstrated that ZnO, which forms the zinc blende structure, and CuO, which forms the tenorite structure, simultaneously dissolved into the rock salt structure when combined in equimolar proportions with NiO, MgO, and CoO, which favor the rock salt structure. Subsequent studies provided insight into properties such as decreased thermal conductivity (10) and improved creep resistance (11), as well as lattice strain that resulted from the incorporation of species with different sizes into the cation sublattice (12, 13). Research has also extended the entropy stabilization approach to other classes of ceramics including perovskites (14), zirconates (15), and silicides (16).

The present review focuses on recent progress in computational and experimental studies of high-entropy borides (HEBs) and carbides (HECs). Please note that throughout the review, we use the convention suggested by Miracle & Senkov (17) whereby elements are listed in alphabetical order.

2. COMPUTATIONAL STUDIES

Several excellent reviews have discussed the discovery, synthesis, properties, and applications of a broad range of high-entropy ceramics including oxides, carbides, diborides, silicides, and nitrides (18, 19). Rather than repeat information from these reviews, we focus on two classes of materials that have been explored in response to the need for new materials for ultra-high-temperature environments, HECs, and HEBs (20). The discussion below is organized by concept rather than material class or computational method and is not intended to be a comprehensive review of the literature. Instead, examples are used to illustrate major areas in which theory and computation have added to the understanding, prediction, and synthesis of these materials.

The challenges in predicting the properties of high-entropy materials become apparent with a few back-of-the-envelope calculations. For example, five refractory metals, Ta, Hf, Nb, Zr, and Ti, form rock salt carbides with melting points above 3,100°C. To be thermodynamically stable, the free energy of a single-phase, five-metal-cation HEC must have a lower free energy than the five binary carbides formed by each metal, the 10 ternary carbides formed by the metals taken two at a time, and the 15 carbides formed by taking the metals three and four at time, for a total of 30 carbides. This does not count the myriad off-stoichiometric carbide compositions and the other possible noncarbide structures. Add three additional carbide-forming elements, e.g., V, W, and Mo, and the number of five-element carbide compositions is 56, each of which has a set of competing structures. Similarly, a carbon vacancy in a five-metal HEC has 210 possible compositions in its first neighbor shell, which goes up to over 10^5 when also considering a second shell of cations. Furthermore, studies have shown that elements can be incorporated into rock salt oxides in roughly equimolar proportions that would not otherwise adapt to the underlying crystal structure, i.e., the entropy effects promote solubility of other elements in these structures (21, 22). Clearly, the number and potential complexity of these structures are daunting but at the same time point toward unprecedented potential for materials design.

2.1. Phase Stability

An obvious starting point for characterizing phase stability is to identify the phase within a given composition with the lowest Gibbs free energy compared to all competing phases. The calculation of phase diagrams (CALPHAD) method is designed to do this using a large database of experimental and computational thermodynamic relations. The challenge for high-entropy ceramics is the large number of phases—starting with the binaries and moving up in compositional space—for which accurate data are needed. This challenge led to other approaches for predicting phase stability.

A number of descriptors have been proposed as surrogates for thermodynamic stability. Borrowing concepts from other high-entropy materials, Gild et al. (23) used average differences in the c and a lattice constants of binary metal borides to predict which combinations of metals would form a single-phase high-entropy structure. They noted that the boron sublattice constrains in-plane distortions, which led to relatively small average differences in the a direction. However, of the seven compositions studied, the phase with the largest average difference in the c direction did not form a single phase. They also noted that small average differences in lattice constants may be necessary, but not sufficient, to predict high-entropy phase stability and that other factors such as the stability of alternate phases also need to be considered.

Ye et al. (24) and Jiang et al. (25) used first principles methods to characterize enthalpies of formation and mixing, mixing entropy, and mechanical stability for three different four-cation HECs, (Hf,Ta,Ti,Zr)C, (Hf,Nb,Ta,Zr)C, and (Nb,Ti,V,Zr)C. In each case, structural stability with respect to shear and negative formation energies was reported, with Ye et al. also reporting measured thermal conductivity, hardness, elastic modulus, and fracture toughness for (Nb,Ti,V,Zr)C. Similar calculations were performed by Zhang et al. (26) for (Hf,Nb,Ta,Ti,Zr)C.

Curtarolo and colleagues (27) developed a different descriptor for thermodynamic stability for high-entropy ceramics called entropy forming ability (EFA) that takes advantage of an efficient, high-throughput first principles methodology. In this approach, the smallest unit cell that can accommodate the composition being explored is determined, and energies for all configurations within a given unit cell size are calculated. For example, a five-cation, cubic carbide structure can be described by a 10-atom unit cell. The EFA is then defined as the inverse of the standard deviation of the distribution of calculated energies. Rather than identify this quantity with phase stability,

they use this to quantify the synthesizability of a given composition. This approach was used to screen the 56 possible five-metal cubic carbide compositions for eight refractory metals, Ta, Zr, Hf, V, Ta, Mo, W, and Nb. Compositions with the largest EFA values formed single phases, while those with lower values formed multiple phases. Advantages to this approach are that temperature is not treated explicitly, which can be a challenge for first principles methods; it is well adapted to high-throughput calculations; and it is relatively straightforward to calculate.

Vecchio, Curtarolo, and coworkers (28) developed a machine learning algorithm for predicting EFA values and, hence, synthesizability that was intended to explore composition space more efficiently than can be done with density functional theory (DFT) calculations. Two training sets were developed: one that used a set of physical properties such as ionic character and valence electrons and one that added CALPHAD data. The algorithm was then used to find EFA values for 70 compositions containing chromium, an element that was not in the original set of DFT calculations. Calculations were validated by synthesizing select compositions based on predicted EFA values.

The EFA approach is being extended to more generally predict stable high-entropy materials across the periodic table (29). One challenge is the ability to calculate accurate energies for oxides, borides, and nitrides (30), which are materials of interest within the emerging high-entropy ceramics community. One of the reasons that the method works for carbides is that the enthalpy landscape is relatively flat (29). For nitrides and borides, however, the reference energies can be very different (for example, di- versus monoboride references), so information regarding appropriate reference structures and energies is needed in addition to the EFA to characterize a given composition.

2.2. Electronic Structure and Mechanical Properties

Bond strengths in carbides, as well their mechanical and thermal properties, are related to electronic structure, and so it is useful to discuss how these concepts can predict HEC properties. A generic electronic density of states schematic that illustrates several common features of rock salt carbides is shown in **Figure 1**. The carbon s states in energy range I are well below the Fermi level. The largest contribution to electron density comes from the hybridized carbon p and metal d states in energy range II. Energy range III is primarily due to metal d states. This electronic structure results in a deep pseudogap that separates lower energy bonding states from higher energy

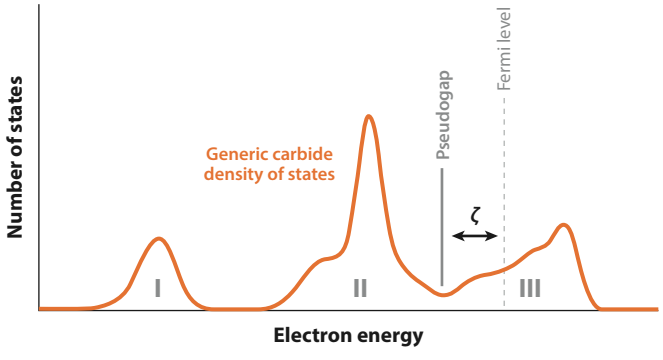

Figure 1

Illustration of the electronic density of states for a generic carbide showing three energy ranges: I, from carbon s states; II, from hybridized carbon p and metal d states; and III, from metal d states.

antibonding states. The closer the Fermi level is to the pseudogap, the fewer antibonding states that are occupied, and the stronger the covalent bonds are in the structure. For traditional carbides, the Fermi level and, therefore, the bonding properties can be tailored by adding other elements. For example, WC can be hardened by adding Re (31). For HECs, this same concept can be used to design materials with desirable properties and tunable covalent bond strengths, as discussed below.

Theory and computation also suggest that the location of the Fermi level relative to the pseudogap affects phonon-electron scattering and the relative contributions of electrons and phonons to thermal conductivity (32). This effect, combined with the stronger covalent bonding also associated with the Fermi level being at the pseudogap, contributes to enhanced phonon conductivity at high temperatures.

The hardness of transition metal (TM) rock salt carbides and carbonitrides is related to their valence electron concentration (VEC), with the hardness being maximized for a VEC of ~8.4 valence electrons per unit cell (33). To explain this observation, Cohen and colleagues (34) used first principles methods to characterize the relationship between the band structures and C_{44} shear moduli for a series of metal-C_xN_{1-x} rock salt compositions with varied VECs. The calculations predicted a maximum in shear modulus for VEC between 8.3 and 8.5. By analyzing changes in the band structure with shear, they identified a mechanism that accounts for this observation. Energy bands near the Fermi level split, in order of lowest to highest energy, into two bands with primarily p-d π bonding, a band with p-d σ bonding, and a band with d-d metallic bonding. The energy of the p-d σ bonded band increases with shear, hence resisting shear deformation, while the energy of the highest energy band representing d-d metallic bonding decreases with shear deformation. The shear modulus increases with increasing VEC until the p-d σ band is fully occupied, which occurs for a VEC of ~8.4, and then decreases with filling of the d-d metallic bonding band with higher VEC values. Correspondingly, the ductility and toughness increase with increasing VEC above 8.4. This concept is particularly valuable to the degree that band structure is independent of cation identity because the valence electrons associated with atoms in the structure are known and apparently additive in determining the VEC for a given composition.

Balasubramanian et al. (35) used first principles calculations and theory to characterize the relationship between VECs and mechanical properties for a series of carbonitrides. By calculating Pugh's ratio (ratio of bulk to shear moduli) and Poisson's ratio as a function of VEC, they were able to identify a ductile-to-brittle transition that occurs at a VEC of ~10. Like previous work, they found a mechanical instability for VEC greater than ~11 associated with C_{44} becoming negative for all but a few structures. However, they also note that C_{44} becomes positive again starting at about VEC = 14, after which the modulus remains relatively constant with increasing VEC. They attributed this to the filling of electron energy bands with increasing VEC that respond differently to shear. They also noted a monotonic increase in bulk modulus and decrease in hardness with increasing VEC over the range 8 to 11. Elastic modulus was found to be constant for VECs between 8.0 and ~9.5, but then decreased to ~11.0.

Both experiment and computation suggest that VEC concepts are applicable to HECs. Harrington et al. (36) measured the hardness and elastic modulus of a series of seven single-phase HECs using nanoindentation and compared the values to rule-of-mixtures estimates. These compositions had VEC values between 8.2 and 9.4. Consistent with the analysis discussed above, the hardness decreased with increasing VEC. The elastic modulus, however, increased with VEC, with a maximum at VEC = 9.4. Without experimental data on materials with higher VECs in which elastic modulus is predicted to decrease sharply with increasing VEC, determining whether measured values correspond to the predicted plateau region is difficult. The HECs used in experiments may also contain carbon vacancies, stacking faults, or other defects that might change the elastic

Table 1 Valence electron concentration, energy differences between the Fermi level and pseudogap (ζ), lattice constants, and bulk moduli for binary carbides

Group	Compound	Valence electron concentration	Binary carbide ζ (eV)	Lattice constant (Å)	Bulk modulus (GPa)
IV	TiC	8	0.0508	4.33	245
	ZrC	8	0.07	4.67	222
	HfC	8	0.00338	4.65	241
V	VC	9	1.32	4.16	300
	NbC	9	1.82	4.48	288
	TaC	9	1.42	4.48	317
VI	MoC	10	2.65	4.37	348
	WC	10	3.13	4.39	350

Shading emphasizes the groupings based on the column in the periodic table and the corresponding valence electron concentration.

modulus. For both the hardness and elastic modulus, the measured values for HECs were greater than those expected from a rule of mixtures.

The VEC, the energy difference between the Fermi level and the pseudogap (ζ) given by DFT calculations, and the bulk modulus from DFT for eight refractory metal binary carbides are given in **Table 1** (37). For VEC = 8, the Fermi energy is approximately in the pseudogap, and the materials have strong covalent bonds. As VEC increases, states with metallic character begin to fill, and the ζ values get correspondingly larger, as expected. In addition, the bulk moduli increase with increasing VEC, again consistent with prior analyses (35). Note also that no overlap exists for values between the group IV, V, or VI elements for both ζ and bulk modulus (e.g., all bulk modulus values for the group V elements are larger than those for group IV and smaller than those for group VI).

The VEC values, ζ values taken as averages of the binary in each composition and directly from DFT calculations (37), and bulk moduli again taken as averages of the binary in each composition and directly from DFT calculations for nine compositions of five metal HECs are compared in **Table 2**. Seven of these correspond to compositions that were studied by Harrington et al. (36). Several trends are apparent. First, like the binaries, larger VEC values for HECs correspond to larger ζ values and more filled metallic states. In addition, like the binaries, no overlap exists for ζ values between groupings by VEC. Second, ζ values calculated as averages of the binaries for a given HEC follow the same trends as those obtained from direct DFT values, with the DFT values being uniformly larger than the binary averages. Hence, HECs are predicted to have more metallic bonding than the average of their constitutive binaries. Third, bulk modulus tends to increase with increasing VEC and ζ, consistent with prior analyses; bulk modulus is also reasonably well approximated by the binary averages. The values are also uniformly lower than the experimental values reported by Harrington et al. (36). Like the binaries in **Table 1**, no overlap in bulk modulus values was observed for different VEC regions. However, overlap is apparent in the ranges of bulk modulus values for the shaded regions for direct DFT calculations. Hence, while binary averages are, in general, reasonable approximations to full calculations and follow expected trends, other effects may be present in DFT data that are not reproduced with binary averaging.

From the discussion above, the chemical bonding characteristics and mechanical properties arising from electronic structure in carbides can be largely captured by a few parameters such as the VEC and ζ values. Furthermore, by definition, VEC is additive from the atoms, and first

Table 2 Valence electron concentration, energy differences between the Fermi level and pseudogap (ζ), and bulk moduli for high-entropy carbides

Composition	VEC	Binary average ζ (eV)	DFT calculation ζ (eV)	Binary average (GPa)	Bulk modulus (GPa)
$(Hf_{0.2}Nb_{0.2}Ta_{0.2}Ti_{0.2}Zr_{0.2})C$	8.4	0.67	0.88	263	266
$(Hf_{0.2}Nb_{0.2}Ta_{0.2}Ti_{0.2}V_{0.2})C$	8.6	0.92	1.01	279	280
$(Hf_{0.2}Nb_{0.2}Mo_{0.2}Ta_{0.2}Ti_{0.2})C$	8.6	0.94	1.11	275	280
$(Hf_{0.2}Mo_{0.2}Ti_{0.2}W_{0.2}Zr_{0.2})C$	8.8	1.18	1.26	282	275
$(Hf_{0.2}Nb_{0.2}Ta_{0.2}Ti_{0.2}W_{0.2})C$	8.8	1.28	1.48	289	284
$(Hf_{0.2}Mo_{0.2}V_{0.2}W_{0.2}Zr_{0.2})C$	9.0	1.43	1.56	292	278
$(Hf_{0.2}Mo_{0.2}Ta_{0.2}W_{0.2}Zr_{0.2})C$	9.0	1.43	1.64	296	286
$(Hf_{0.2}Ta_{0.2}Ti_{0.2}W_{0.2}Zr_{0.2})C$	9.0	1.55	1.77	300	323
$(Mo_{0.2}Nb_{0.2}Ta_{0.2}V_{0.2}W_{0.2})C$	9.4	2.07	2.1	320	325

Abbreviations: DFT, density functional theory; VEC, valence electron concentration.
Shading emphasizes the five groupings based on VEC values.

principles computations suggest that both the ζ values and bulk moduli for HECs are reasonably additive from the binaries. It is therefore instructive to see what other quantities might also be additive from the binaries. This not only is useful for quick property estimates, but also speaks to the uniqueness of these materials: Are properties additive from a rule of mixtures, or does the large number of species lead to unpredictable characteristics? Lattice constants and cohesive energies (defined as the energy needed to separate atoms to infinity) are plotted in **Figure 2** for the set of compositions in **Table 2**. Values were calculated by averaging predictions from direct DFT calculations for the constitutive binaries. Clearly, this limited set of properties is predicted reasonably well from a rule of mixtures based on binary carbide compositions. The degree to which other properties, such as thermal and electrical conductivities, thermal expansion, and other elastic constants, are also binary additive is an area for further exploration.

Most prior studies of mechanical properties in carbides used ternary compositions to manipulate the VEC, for example, changing the carbon and nitrogen ratios with one type of metal cation or varying two cations within either a carbon or nitrogen sublattice. Studies have also noted that carbon forms stronger covalent bonds than nitrogen in these compositions (38). The ability to incorporate multiple cations within a carbide composition, including species that otherwise would not have formed such a structure, provides another level of flexibility in designing materials with specific properties.

Unifying theoretical and computational concepts such as those discussed above for carbides are, in general, not as well developed for HEBs, and much of what has been done has not yet been applied to borides. Instead, much of the theoretical and computational work in this area has focused on areas such as searching for superhard materials and materials for harsh environments, as well as specific deformation mechanisms and slip activity (39). This is a fertile area for computation as the field of high-entropy ceramics evolves.

2.3. Thermal Conductivity

The current understanding of thermal conductivity in high-entropy ceramics is incomplete. In conventional materials, adding disorder reduces electron and phonon scattering lengths, which, in general, lowers thermal conductivities. How these effects are manifested in high-entropy

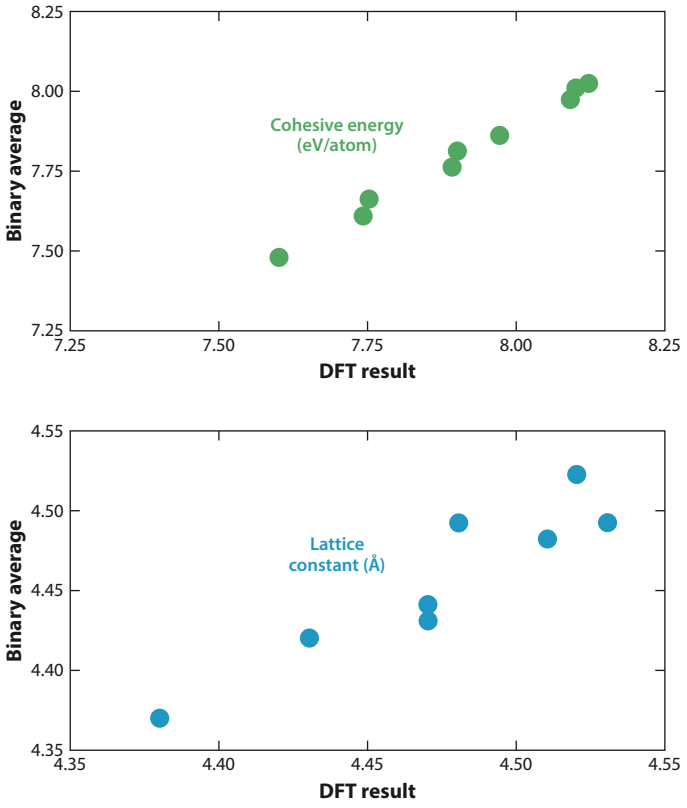

Figure 2

Prediction of cohesive energy (*top*) and lattice parameter (*bottom*) from binary averaging versus direct density functional theory (DFT) for the nine high-entropy carbide compositions summarized in **Table 2**. Note that the lattice parameters for two of the high-entropy carbides are identical and result in overlap of two points at 4.38 Å in the bottom panel.

ceramics, which by definition contain a large amount of disorder, is unclear. For example, changes in thermal conductivity in the high-entropy rock salt oxide (Cu,Co,Mg,Ni,Zn)O was studied as a function of the addition of Sc, Sn, Ge, or Cr in equimolar amounts (40). Traditional theory predicts that phonon scattering due to differences in mass should saturate with respect to the addition of other species at five cations. However, experimental measurements showed further reduction in thermal conductivity with the additional cation species (40). Molecular simulation and theory showed that the additional loss of phonon thermal conductivity was primarily due to additional disorder in the interatomic forces from charge transfer and equilibration, not mass scattering (24, 41). For example, based on its smaller mass, Sc should increase thermal conductivity when added in an equimolar amount. However, Sc has a +1 oxidation state that requires charge transfer to be accommodated. This charge transfer and the resultant changes in interatomic forces lower the thermal conductivity (42).

Dai et al. (43) reported a series of classical molecular dynamics simulations of (Hf,Nb,Ta,Ti,Zr)C using a deep learning interatomic potential. The simulations calculated a number of temperature-dependent properties, including the lattice constant (i.e., thermal expansion), elastic constants, and phonon-mediated thermal conductivity. The last, which was

calculated with an equilibrium Green-Kubo method using classical trajectories, varied from 2.02 W/(m·K) at 0°C to 0.95 W/(m·K) at 2,400°C. These are relatively low thermal conductivities, consistent with the disorder in the system, but lower than experimental measurements of ~6.5 W/(m·K) (10, 44). Because HECs are metallic conductors, the difference between the simulated phonon-mediated thermal conductivity and measured values may be the electron contribution to thermal conductivity. Rost et al. (44) reported measurements of total thermal and electrical conductivities of films of this same composition as a function of carbon content. These studies also report a total thermal conductivity of ~6.5 W/(m·K). By converting the electrical to thermal conductivity via the Wiedemann-Franz law, Rost et al. determined that the relative electron and phonon contributions varied widely with carbon content, but for full carbon stoichiometry, as studied in the molecular dynamics simulations, a majority of thermal conductivity was likely due to phonons. Hence, simulations appear to underestimate phonon thermal conductivity. This discrepancy could arise from several factors, such as nonlinearity in the interatomic forces that is large compared to the true system. Clearly more research is needed from both experiment and computation to better understand thermal transport in these materials.

Theory and computation are working closely with experiment both to design new compositions with potentially interesting and useful properties and to better understand the origin and prediction of these properties. This field is in its infancy, and while accepted theory and modeling on related compositions provide a good starting point for high-entropy materials, many avenues need to be explored further.

3. EXPERIMENTAL STUDIES

This section is organized based on the two major crystal structures of high-entropy UHTCs (HE-UHTCs). Section 3.1 describes HEBs with the AlB_2 structure. Section 3.2 focuses on HECs with the rock salt structure. Both HEBs and HECs exhibit wide ranges of solubility for various TMs on the metal sublattice.

3.1. High-Entropy Boride Ceramics

The behavior of HEBs is based on that of group IV borides, namely, TiB_2, ZrB_2, and HfB_2. These compounds form line compounds with a B-to-TM ratio of 2 and no significant vacancy formation. This section assesses the synthesis, densification, properties, and oxidation behavior of HEBs.

3.1.1. Synthesis. The most common synthesis method is solid solution (SS) formation using commercial diboride powders. The first report of HEB synthesis included $(Hf,Nb,Ta,Ti,Zr)B_2$, $(Hf,Mo,Ta,Ti,Zr)B_2$, $(Hf,Mo,Nb,Ti,Zr)B_2$, $(Hf,Mo,Nb,Ta,Ti)B_2$, and $(Mo,Nb,Ta,Ti,Zr)B_2$ that were produced using high-energy ball milling (HEBM) of individual commercial diboride powders followed by spark plasma sintering (SPS) at 2,000°C (23). The HEBM process increases surface area and promotes homogeneous mixing, but it also introduces surface oxides on particle surfaces and impurities associated with wear of the milling media (45). Borothermal reduction (BTR) and boro-carbothermal reduction (BCTR) have also been widely used to synthesize HEB powders. Reactions 1–3 show examples for the formation of ZrB_2 (46–48).

$$3ZrO_{2(s)} + 10B_{(s)} \rightarrow 3ZrB_{2(s)} + 2B_2O_{3(l)}, \quad 1.$$

$$ZrO_{2(s)} + 2C_{(s)} + 2B_{(s)} \rightarrow ZrB_{2(s)} + 2CO_{(g)}, \text{ and} \quad 2.$$

$$7ZrO_{2(s)} + 5B_4C_{(s)} \rightarrow 7ZrB_{2(s)} + 3B_2O_{3(l)} + 5CO_{(g)}. \quad 3.$$

Zhang et al. (46) synthesized $(Cr,Hf,Ta,Ti,Zr)B_2$, $(Hf,Mo,Nb,Ti,Zr)B_2$, and $(Hf,Mo,Nb,Ta,Ti)B_2$ at 1,600°C for 1 h under vacuum by BTR. The powders had equivalent average particle sizes of less than 500 nm but contained up to 7.7 wt% of oxide impurities due to incomplete reaction and B loss during heating. Similarly, $(Hf,Nb,Ta,Ti,Zr)B_2$, with an average size of ~300 nm, was synthesized by BTR at 1,700°C for 1 h in flowing argon (47). However, unreacted metal oxides remained, and a B_2O_3 layer was detected on HEB particles. Single-phase $(Nb,Ta,Ti)B_2$ powders were produced by molten salt synthesis at 1,100°C using 20–30 wt% excess B (48). The resulting particles were nanorods ~200 nm long with an aspect ratio of ~5. However, filtering and washing were required to remove salt and B_2O_3 from the products, while some compositions contained multiple phases. Single-phase $(Hf,Nb,Ta,Ti,Zr)B_2$ powders with a specific surface area of 1.6 m^2/g were synthesized at 1,850°C under vacuum (10–100 Pa) by BCTR of TM oxides with C and excess B (49). The combination of HEBM and mild vacuum promoted full reaction, but it also led to loss of volatile B-O species. The results from both reports indicate that optimization of starting compositions (e.g., excess B or B_4C), mixing homogeneity, and synthesis conditions (e.g., temperature and atmosphere) are required to achieve full reaction.

The loss of B during synthesis can be compensated for by adding excess B or B_4C (50–52). However, residual B_4C and/or C can be present even when X-ray diffraction (XRD) indicates phase-pure products due to the low X-ray scattering cross sections of light elements. In addition, the minimum temperature for BTR/BCTR to go to completion appears to be ~1,700°C, while formation of single-phase HEB powders appears to require at least 1,800°C. As a result, some researchers consider reduction synthesis to consist of two steps, the first being BTR/BCTR and the second being SS formation (53).

Several alternative methods have been used to synthesize HEBs. Self-propagating high-temperature synthesis (SHS) was used to synthesize $(Hf,Mo,Nb,Ta,Ti)B_2$ and $(Hf,Mo,Nb,Ti,Zr)B_2$ (54, 55). Secondary borides, HfO_2, and unreacted B were detected in the products because the SHS reaction did not reach equilibrium. Reactive SPS was also reported, but the degree of conversion was only ~64 wt% (55). Arc melting (AM) was used to synthesize $(Cr,Hf,Ta,Ti,Zr)B_2$, $(Hf,Ta,Ti,Zr)B_2$, $(Cr,Hf,Ti,Zr)B_2$, $(Cr,Hf,Ta,Zr)B_2$, $(Cr,Hf,Ta,Ti)B_2$, and $(Cr,Ta,Ti,Zr)B_2$ from commercial diborides (56). Oxide impurities were not detected in the final materials, but evaporation and phase segregation were observed.

These reports reveal several key issues for HEB synthesis. First, SS formation using commercial diboride powders typically results in high oxide impurity contents. Minimizing oxygen impurities is critical based on previous boride densification studies that concluded that oxygen contents higher than ~0.5 wt% can inhibit densification (57). Particle size is also a critical factor in subsequent densification, and submicron particles are needed to promote full densification of borides (58). Among the synthesis methods, BCTR of oxides appears to be the most robust route to synthesize nominally phase pure HEB powders with submicron particle sizes, low impurity contents, and low residual oxygen contents. Molten salt synthesis appears promising and has the added benefit of some ability to control particle morphology. Techniques such as SHS and AM have not yet been successful due to issues such as inhomogeneous products or loss of some reactants due to volatilization.

3.1.2. Densification. SPS is the most widely used method to densify HEBs because of enhanced densification attributed to higher heating rates and higher pressures than other methods. The first studies to densify HEBs reached ~92% relative density using mixtures of commercial diboride powders and SPS conditions of 2,000°C and 30 MPa (23), but oxide impurities inhibited densification. SPS was used to densify powders synthesized by SHS but only reached ~92.5%

relative density at 1,950°C and 30 MPa (54, 55). The final ceramics also contained B as a second phase.

Densification of borides can be enhanced by reducing the particle size of the starting powders, which increases surface area and reduces diffusion distances (59–61). $(Hf,Nb,Ta,Ti,Zr)B_2$, $(Cr,Hf,Ta,Ti,Zr)B_2$, $(Hf,Mo,Nb,Ti,Zr)B_2$, and $(Hf,Mo,Nb,Ta,Ti)B_2$ ceramics with relative densities of 95% to 99% were densified by SPS at 2,000°C and 30 MPa from powders with submicron particle sizes (46, 62). However, the final ceramics contained oxide impurities, which resulted in residual porosity in the final ceramics. Oxygen impurity content can be decreased by incorporating reducing agents. For example, HEB powders synthesized at 1,700°C with ~13 wt% excess B_4C that had an oxygen content of ~0.6 wt% and submicron particle size were used to produce $(Hf,Nb,Ta,Ti,Zr)B_2$ ceramics with relative densities up to ~98% (52). However, grains grew from ~7 μm after SPS at 2,000°C to >40 μm after SPS at 2,050°C, emphasizing the need to control processing conditions to control microstructure development. Excess B_4C in BCTR was also used to produce $(Hf,Nb,Ta,Ti,Zr)B_2$, $(Hf,Mo,Ta,Ti,Zr)B_2$, and $(Cr,Hf,Ta,Ti,Zr)B_2$ ceramics that were >99% relative density at 2,000°C under a uniaxial pressure of 80 MPa by SPS due to the lower oxygen contents (51). Nearly fully dense $(Hf,Nb,Ta,Ti,Zr)B_2$ ceramics were produced at 2,100°C under a uniaxial pressure of 50 MPa by a two-step SPS process (63). An isothermal hold at 1,650°C under vacuum was used to promote BCTR and minimize the residual oxygen content. Relative densities increased from 98.9% to 99.9% as the final sintering temperatures increased from 2,000°C to 2,200°C. The high relative densities were attributed to submicron starting particle sizes and low impurity contents (~0.004 wt% oxygen and 0.018 wt% carbon). The average grain size of the HEB ceramics was ~2 μm after densification at 2,000°C and increased to ~5 μm after densification at 2,100°C, but significant grain growth occurred for densification at 2,200°C. The relative densities were higher and residual oxygen contents lower than those of HEBs reported in other studies up to that point (23, 46, 50–52, 62).

HEB ceramics have also been densified by alternative methods such as flash sintering (64, 65). Dense $(Hf,Nb,Ta,Ti,Zr)B_2$ ceramics with an average grain size <20 μm were produced by reactive flash SPS of commercial diboride powders with 3 wt% C (66). Dense HEBs were also produced by AM (56). For AM, all constituents needed to have similar melting points and vapor pressures to produce homogeneous ceramics (56). Notably, CrB_2 was difficult to incorporate by AM because of its lower melting temperature that promoted phase separation and its high vapor partial pressure that led to evaporation. Pressureless sintering has also been used to produce HEBs, but this process produced $(Hf,Nb,Ta,Ti,Zr)B_2$ ceramics that were ~75% dense (67).

Most of the studies to date have discussed densification of HEBs that are nominally single phase, at least by XRD. However, a number of researchers have noted phase segregation in the final HEBs (23, 46, 52, 62, 68–70). Analysis of $(Hf,Nb,Ta,Ti,Zr)B_2$ by XRD was consistent with a ceramic that was nominally single phase, but analysis by scanning electron microscopy (SEM) and energy dispersive spectroscopy revealed the presence of an Nb-rich second phase that appeared as dark regions in SEM (68) (**Figure 3**). The hypothesis was that the Nb-rich regions had the same crystal structure as the main diboride phase with nearly identical lattice parameters. The presence of Nb-rich regions in HEB ceramics could be due to slow diffusion of Nb during SS formation or the presence of a subsolidus miscibility dome.

Several important conclusions can be drawn from the densification studies. First, attaining nearly full relative density is only possible when starting powders have submicron particle sizes and residual oxygen contents <1 wt%. Second, most studies have used SPS for densification, but other methods, particularly hot pressing, should be possible for powders with appropriate particle sizes and oxygen contents. Finally, thorough characterization of densified HEB ceramics is necessary

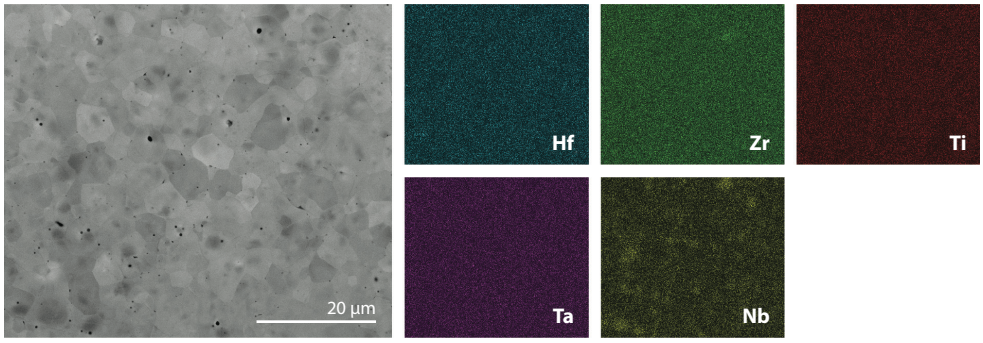

Figure 3

Scanning electron microscopy image and corresponding energy dispersive spectroscopy maps for a $(Ti,Hf,Zr,Ta,Nb)B_2$ ceramic showing the presence of Nb-rich regions. Figure adapted with permission from Reference 68.

to identify oxide impurities, residual C or B_4C, and phase separation that are not always evident in cursory examinations.

3.1.3. Properties. Hardness is the most commonly reported property of HEBs. Values in the range of 17 to 23 GPa were reported using a load of 0.2 kg for ceramics that were ~93% dense (23, 54, 55) and increased to 21 to 29 GPa for higher relative densities (46, 50–52, 62, 63, 68–70). Residual porosity and second phases decrease hardness. As a result, no clear trend is found in hardness as a function of relative density, even when examining just one composition (**Figure 4**) (52, 63). The importance of purity is emphasized by unexpectedly low values of 21.7 ± 1.1 GPa when relative density was 96.3% with 6.4 wt% oxygen (46) and 20.5 ± 1.0 GPa when relative density was 99.5% but B_4C and C were present (51). The indentation size effect has also been

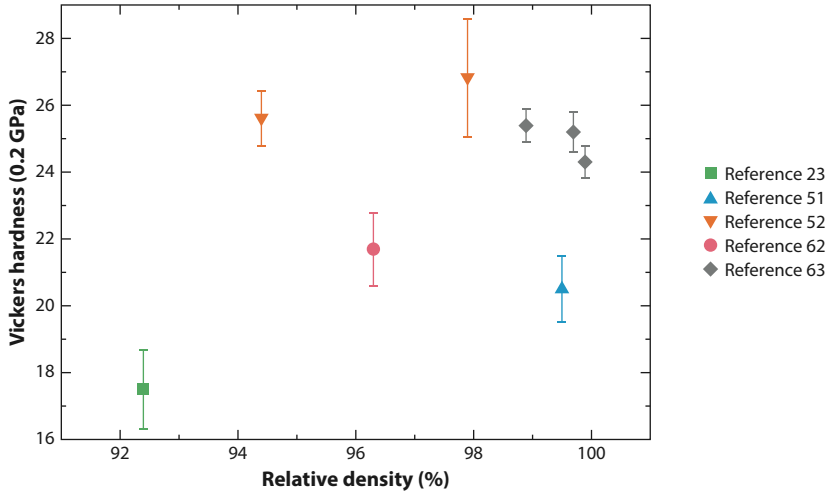

Figure 4

Effect of relative density on Vickers hardness (0.2 kg load) of $(Hf,Zr,Ti,Ta,Nb)B_2$ ceramics plotted using data from References 23, 51, 52, 62, and 63.

demonstrated for HEBs, with the hardness of $(Hf,Nb,Ta,Ti,Zr)B_2$ increasing from 21.0 ± 0.2 GPa at a load of 1 kg to 25.4 ± 0.5 GPa at a load of 0.2 kg (63).

HEBs containing Mo or Cr are harder than other compositions according to Vickers hardness, with the highest HEB hardness to date reported for $(Hf,Mo,Ti,W,Zr)B_2$ at 29.4 ± 1.7 GPa for a load of 0.2 kg (46, 51, 54, 55, 62). The higher hardness of $(Hf,Mo,Ti,W,Zr)B_2$ was attributed to the presence of a W-rich secondary phase. The addition of SiC particles has been reported to increase hardness in ceramics due to a decrease in grain size and increase in relative density (50). The hardness values of fully dense HEBs are higher than predicted from the properties of the constituents using a volumetric rule of mixtures calculation, which has been attributed to disorder among the TM species and SS hardening (23, 71–75).

Young's modulus values of $(Hf,Nb,Ta,Ti,Zr)B_2$ ceramics ranged from 480 to 527 GPa depending on relative density (50, 52). Modulus values decreased to 440–460 GPa when 20 vol% SiC was added because SiC has a lower modulus (~475 GPa) than borides (76). Indentation fracture toughness of HEB ceramics ranged from 2.8 to 4.5 $MPa{\cdot}m^{1/2}$, which is typical of boride ceramics (50, 52, 62). Presumably, the limited number of property studies is due to the small billets that can be produced by SPS in most laboratories.

Room temperature thermal conductivity values were reported to be 25 ± 5 W/(m·K) for $(Hf,Nb,Ta,Ti,Zr)B_2$, 15 ± 4 W/(m·K) for $(Hf,Mo,Ta,Ti,Zr)B_2$, and 13 ± 3 W(m·K) for $(Cr,Hf,Ta,Ti,Zr)B_2$ for dense HEB ceramics (51). The values are lower than any of the constituent borides, which was attributed to increased phonon scattering in the HEBs. The highest thermal conductivity was measured for $(Hf,Nb,Ta,Ti,Zr)B_2$, which was consistent with DFT predictions (77). Thermal properties, including thermal diffusivity, heat capacity, and thermal conductivity, were also reported for porous $(Hf,Nb,Ta,Ti,Zr)B_2$ ceramics (67). The porous HEB ceramics exhibited lower thermal conductivity values than did other UHTCs.

No systematic studies of HEB properties have been reported. Trends related to composition and microstructure-property relationships have not yet been studied. In particular, the lack of measured strength and fracture toughness values stems from the limited specimen sizes that are possible with laboratory-scale SPS systems used for densification.

3.1.4. Oxidation behavior. Most HEB ceramics show lower weight gains than do individual boride ceramics produced with the same processing conditions (23). For example, $(Hf,Mo,Nb,Ta,Ti)B_2$ ceramics exhibited low and stable oxidation rates up to 1,200°C, whereas TiB_2 and TaB_2 had significant weight gains below 700°C. Both analytical and computational thermodynamic approaches were used to investigate the oxidation behavior of $(Hf,Nb,Ta,Ti,Zr)B_2$ ceramics (78, 79). Both experimental results and thermodynamic predictions indicated a tendency toward preferential oxidation of the more reactive species (TiB_2, ZrB_2, and HfB_2) compared to other constituents. As with other properties, systematic studies are needed to identify reaction mechanisms and kinetics, along with the effects of composition on oxidation behavior.

3.2. High-Entropy Carbides

The behavior of HECs is similar to the group IV and V carbides that form the rock salt structure, including ZrC, HfC, and TaC. These compounds are stable for C-to-TM ratios from ~0.6 to 0.98 and form vacancies on the carbon sublattice. This section discusses the synthesis, densification, properties, and oxidation behavior of HECs.

3.2.1. Synthesis. Single-phase HEC powders were synthesized at 1,950°C by SS formation using commercial carbide powders (80). Mechanical milling (MM) of metal powders and graphite

for 3,000 min was used to form HEC powders at room temperature (81). The resulting powders had a crystallite size <300 nm but had significant Fe contamination. Both SS and MM methods typically result in high levels of impurities, which are inherent to the starting materials and/or are introduced by milling. Higher purity HEC powders with finer particle sizes can be produced by carbothermal reduction (CTR). For example, CTR reactions are complete at ~1,600°C and SS formation is complete at ~1,900°C when using HEBM of oxides and carbon black (82). Likewise, chemical methods can be used to produce HECs with high purity (83). Oxides were produced as an intermediate product, but CTR reactions were complete at 1,400°C due to the more intimate mixing of the reactants in solution. Although significant SS formation occurred below 1,700°C, formation of a single-phase SS required heating to 1,900°C. Hence, formation of single-phase HEC powders appears to be controlled by temperature, regardless of the scale of mixing. This behavior could be due to different diffusion rates for the different carbide constituents based on a study that surmised that the relative diffusion rates were TaC < ZrC ~ HfC < NbC < TiC (84). Single-phase HECs can be synthesized by a variety of methods, and removal of oxygen impurities appears to be less difficult than with HEBs. This could be due to oxygen solubility in the carbides (i.e., trace oxide impurities may dissolve into the lattice rather than being trapped at grain boundaries and triple grain junctions) and/or the wider range of stoichiometry possible in carbides (i.e., carbon in excess of the minimum required for conversion of oxide to carbide may dissolve into the lattice).

3.2.2. Densification. The most common densification route for HECs is SPS. Relative densities of ~99% or above are typically produced by SPS at 2,200°C or 2,300°C (27, 36, 84). Most compositions appear to form single-phase HECs with the rock salt structure, although compositions containing Mo and W have been noted to form second-phase carbides (36). Densification at lower temperatures produces porous HECs that have phase segregation (85). Likewise, reactive flash SPS can be used to produce dense HECs, but the one reported study found residual graphite and oxides in the final ceramic, indicating that CTR did not go to completion (66). Finally, one study reported pressureless sintering, which also resulted in a porous HEC (86).

The use of in situ reaction/densification processes can improve densification compared to SS formation using individual carbide powders. HEC ceramics with a relative density of ~98% were produced by reacting metals with C, but neither Zr nor Nb was uniformly distributed due to oxidation and self-ignition of metal powders (87). Dense HECs can also be produced from powders produced by CTR (87–90). The results indicate that single-phase HECs are difficult to produce when CTR and SS formation are combined into a single step, potentially because of the large amount of CO gas formed by CTR. Two-step processes that use separate CTR and SS/densification steps are more successful at producing dense, single-phase HECs (90).

Full densification of HECs is possible at temperatures as low as 1,850°C with submicron particles with oxygen contents below 1 wt%. As with HEBs, oxide impurities suppress densification of HEC ceramics. These impurities are due to intrinsic surface oxides and/or additional oxides introduced during milling. Hence, production of dense HECs is difficult to achieve with commercial carbide starting powders because of the inherent impurity levels and required comminution and mixing steps. Combined processes that directly synthesize submicron particles and densify them without additional processing steps are a facile method to produce fully dense HECs. As with HEBs, fundamental studies of sintering mechanisms and kinetics are lacking.

3.2.3. Properties. Hardness and modulus have been the most reported HEC properties, with many studies using nanoindentation. Because of the small indent sizes, nanohardness is higher than microhardness, and indents are smaller than individual grains so nanohardness is not affected by

porosity. Nanohardness for (Hf,Nb,Ta,Zr)C was 36.1 ± 1.6 GPa at loads of 50 and 300 mN (84). The HEC hardness was higher than that of any of the constituent carbides and ~30% higher than the value of 27.7 GPa estimated by a volumetric rule of mixtures calculation, which was attributed to SS hardening affecting slip behavior and elastic constants. Other studies reported nanohardness values ranging from 27 to 32 GPa at a load of 100 mN for a variety of HEC compositions, which were also higher than values estimated from the properties of the constituent carbides and attributed to inhibition of dislocation movement by mass disorder (27, 36). Other researchers have attributed enhanced hardness to the size mismatch among the TMs, which results in lattice distortion that limits the motion of dislocations necessary for plastic deformation and changes the slip systems and the ease with which slip can occur (84, 91). Nanohardness values as high as 40.6 ± 0.6 GPa have been reported but are likely due to the smaller indentation loads (27, 36). Unlike nanohardness, microhardness is affected by residual porosity. For example, (Hf,Nb,Ta,Ti,Zr)C ceramics with a relative density of 93% had Vickers hardness of 15 GPa at a load of 1 kg (10), while hardness increased to 18.8 ± 0.4 GPa for a relative density of 95.3% (85) and 24.4 ± 0.5 GPa for a density of >99% (90). Hardness is a convenient property to measure, but the indentation type, relative density, and load must be taken into account for comparison.

Modulus values measured by nanoindentation have ranged from ~440 GPa up to nearly 600 GPa (10, 27, 36, 84, 85) compared to values in the range of ~400 to ~450 GPa measured by ultrasonic methods (89). Indentation fracture toughness was 3.0 ± 0.2 $MPa{\cdot}m^{1/2}$ for (Hf,Nb,Ta,Ti,Zr)C (85) and 3.3 ± 0.1 $MPa{\cdot}m^{1/2}$ for (Mo,Nb,Ta,Ti,Zr)C (87). Single-edge notched beam toughness ranged from 4.9 to 5.9 $MPa{\cdot}m^{1/2}$ (92), while using chevron notch beams the value was 3.5 ± 0.3 $MPa{\cdot}m^{1/2}$ for (Hf,Nb,Ta,Ti,Zr)C (93). Toughness values for HECs are close to values reported for individual carbides, indicating that SS may not affect fracture toughness. The flexure strength for (Hf,Nb,Ta,Ti,Zr)C ceramics with relative densities ranging from 92.7% to 94.9% ranged from 318 to 400 MPa in three-point bending (92). (Hf,Nb,Ta,Ti,Zr)C ceramics with relative densities >99.0% had a room temperature strength of 421 ± 27 MPa (93). Higher strengths were achieved due to the higher relative densities. With increasing temperature, strength stayed above ~400 MPa up to 1,800°C, then decreased to 318 ± 21 MPa at 2,000°C and 93 ± 10 MPa at 2,300°C. The decrease in strength above 1,800°C was consistent with a decrease in dislocation density, which could also be related to other effects, such as creep deformation or reduction in elastic modulus with increasing temperature. These are initial reports of HEC strength, and further systematic studies are needed to determine the effects of composition, grain size, impurities, and relative density on mechanical properties.

Very few studies have reported the thermal properties of HEC ceramics. Room temperature thermal diffusivity of 3.6 mm^2/s and thermal conductivity of 6.5 W/(m·K) were reported for (Hf,Nb,Ta,Ti,Zr)C ceramics with a relative density of 93% (10). Both are much lower than reported for the individual carbides, which was attributed to enhanced scattering of phonons and electrons by metals of different masses in the lattice (10, 86). Interestingly, the thermal conductivity of (Hf,Nb,Ta,Ti,Zr)C with a relative density of ~19% was 0.4 W/(m·K) at 29.5°C, which is only 1/20 of the dense HEC ceramic (86). Obviously, more studies are needed to determine compositional dependency and the mechanisms that control the thermal conductivity of HEC ceramics.

3.2.4. Oxidation resistance. Thermal gravimetric analysis combined with differential scanning calorimetry showed that mixed individual carbide powders started to oxidize at 200°C, whereas HEC powders did not start to oxidize until ~400°C (80). The mixed powders showed clear step-by-step oxidation, indicating that individual components were oxidized separately as temperature increased. In contrast, the HEC powders reacted to form a poorly crystalline oxide up to ~800°C.

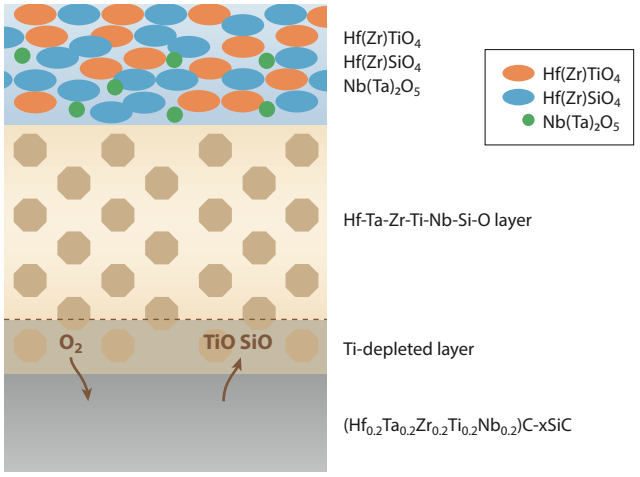

Figure 5

Schematic illustration of the oxidation mechanism proposed for (Hf,Ta,Zr,Ti,Nb)CSiC ceramics. Figure adapted with permission from Reference 97.

Between 800°C and 1,400°C, the oxidation rate of mixed powders increased, whereas the oxide products formed on the HEC powders began to decompose. Above 1,400°C, both materials oxidized to the same complex mixture of oxides. Hence, the complex HEC improved oxidation resistance, at least in the intermediate temperature range.

Parabolic rate constants were measured for (Hf,Nb,Ta,Ti,Zr)C ceramics that were oxidized in air up to 1,200°C (94). A dense oxide layer was formed up to ~900°C, but the oxide spalled at higher temperatures. Parabolic oxidation kinetics were observed for (Hf,Nb,Ta,Ti,Zr)C ceramics up to 1,500°C in air (95). However, paralinear kinetics were observed at higher temperatures due to loss of protection. A triple-layered structure was observed after oxidation at 1,400°C, which was attributed to a mechanism controlled by the inward diffusion of O_2 and the outward diffusion of Ti and CO. Oxidation of (Hf,Nb,Ta,Ti,Zr)C ceramics in water vapor at 1,200°C showed the formation of a protective scale (96). Finally, the oxidation of an HEC containing SiC found parabolic mass gain kinetics up to 1,500°C in air, which was attributed to the formation of protective Hf(Zr)SiO_4 and Hf(Zr)TiO_4 layers (**Figure 5**) (97). The process was controlled by the outward diffusion of TiO. Results to date indicate that the high-entropy effect can improve oxidation behavior, particularly at temperatures below ~1,400°C.

4. CURRENT STATUS AND FUTURE OPPORTUNITIES

HE-UHTCs have emerged as an exciting research area that has increased interest in the area of materials for extreme environments. The complex compositions of HE-UHTCs present challenges for both computational and experimental studies. Computationally, the large number of chemical species result in a large number of unique bonding environments that require large numbers of computations to model the behavior of HEBs and HECs. To date, computational studies have been successful in designing new compositions, describing the ability to form specific compositions, and predicting properties such as elastic modulus. However, further research is needed to extend computational methods to more complex problems such as thermal transport and oxidation. Experimental studies have demonstrated a variety of synthesis methods and have been able to

produce dense HEBs and HECs. In particular, two-step processes that use reaction-based methods to synthesize submicron particles followed by densification have been used to produce dense HEBs and HECs with high phase purity and controlled microstructure development. Challenges remain in areas such as composition-microstructure-property relationships and fundamental studies of kinetic processes and phase stability.

Looking forward, several areas have been identified as areas where in-depth research is needed to enhance the understanding of HE-UHTCs.

- Computations should be extended to more complex structures that account for the variety of bonding and nearest neighbor environments for the various species in HE-UHTCs. For example, complexity of the nonmetal sublattice has not been explored. Likewise, analysis of nearest neighbor and next-nearest neighbor effects is also needed.
- Properties such as thermal conductivity, electrical conductivity, and thermal expansion have not been accurately predicted computationally. In addition, the fundamental reasons for differences between properties predicted from averages of constituents and those measured for high-entropy ceramics have not been explored in sufficient depth to identify the atomistic or electronic structure effects responsible for the differences.
- Experimental studies of composition-microstructure-property relationships are needed to elucidate the intrinsic mechanical behavior and oxidation response. In addition, detailed characterization of structures is needed to determine distribution of elements in these compositionally complex materials as well as the effects that various species have on the local bonding environment (e.g., bond type, strength, and length).
- Fundamental physical and chemical property studies are needed. For example, the phase equilibria and thermodynamic properties need to be studied experimentally. Not only are these important for predicting thermochemical stability and designing microstructures, but they are also needed for verification of computational models. In addition, kinetic studies of densification and oxidation are lacking. Finally, analysis of phonon and electron transport processes are needed to identify mechanisms controlling properties such as thermal diffusivity and electrical conductivity.
- The mechanisms of synthesis reactions and densification processes need to be elucidated to enable scale-up. To date, most studies have produced just a few grams of powder or dense cylindrical billets on the order of 25 mm in diameter and a few millimeters thick. Knowledge of mechanisms will allow for scaling powder synthesis and densification methods to produce larger ceramics without problems such as higher impurity levels, nonuniform microstructures, or other inhomogeneities.

DISCLOSURE STATEMENT

The authors are not aware of any affiliations, memberships, funding, or financial holdings that might be perceived as affecting the objectivity of this review.

ACKNOWLEDGMENTS

The contributions of L.F. were supported by the Enabling Materials for Extreme Environments signature research area. Support for W.G.F. was provided by the National Science Foundation through grant CMMI-1902069. D.W.B. was supported by a Multi-Disciplinary University Research Initiative through award N00014-15-1-2863 from the Office of Naval Research.

LITERATURE CITED

1. Wuchina EJ, Opila E, Opeka MM, Fahrenholtz WG, Talmy IG. 2007. UHTCs: ultra-high temperature ceramic materials for extreme environment applications. *Interface* 16:30–36
2. Fahrenholtz WG, Hilmas GE, Talmy IG, Zaykoski JA. 2007. Refractory diborides of zirconium and hafnium. *J. Am. Ceram. Soc.* 90:1347–64
3. Fahrenholtz WG. 2014. A historical perspective on research related to ultra-high temperature ceramics. In *Ultra-High Temperature Ceramics: Materials For Extreme Environment Applications*, ed. WG Fahrenholtz, EJ Wuchina, WE Lee, Y Zhou, pp. 6–32. New York: Wiley
4. Cantor B, Chang ITH, Knight P, Vincent AJB. 2004. Microstructural development in equiatomic multicomponent alloys. *Mater Sci. Eng. A* 375–77:213–18
5. Yeh J-W, Chen S-K, Lin S-J, Gan J-Y, Chin T-S, et al. 2004. Nanostructured high-entropy alloys with multiple principal elements: novel alloy design concepts and outcomes. *Adv. Eng. Mater.* 6:299–303
6. Tsai M-H, Yeh J-W. 2014. High-entropy alloys: a critical review. *Mater. Res. Lett.* 2:107–23
7. Senkov ON, Wilks GB, Scott JM, Miracle DB. 2011. Mechanical properties of $Nb_{25}Mo_{25}Ta_{25}W_{25}$ and $V_{20}Nb_{20}Mo_{20}Ta_{20}W_{20}$ refractory high entropy alloys. *Intermetallics* 19:698–706
8. Otto F, Yang Y, Bei H, George EP. 2013. Relative effects of enthalpy and entropy on the phase stability of equiatomic high-entropy alloys. *Acta Mater.* 61:2628–38
9. Rost CM, Sachet E, Borman T, Moballegh A, Dickey EC, et al. 2016. Entropy-stabilized oxides. *Nat. Commun.* 6:8485
10. Yan X, Constantin L, Lu Y, Sivain J-F, Nastasi M, Cui B. 2018. $(Hf_{0.2}Zr_{0.2}Ta_{0.2}Nb_{0.2}Ti_{0.2})C$ high entropy ceramics with low thermal conductivity. *J. Am. Ceram. Soc.* 101:4486–91
11. Han X, Girman V, Sedlak R, Dusza J, Castle EG, et al. 2020. Improved creep resistance of high entropy transition metal carbides. *J. Eur. Ceram. Soc.* 40:2709–15
12. Rak Z, Maria JP, Brenner DW. 2018. Evidence for Jahn-Teller compression in the (Mg,Co,Ni,Cu,Ni)O entropy-stabilized oxide: a DFT study. *Mater. Lett.* 217:300–3
13. Berardan D, Meena AK, Fanger S, Herero C, Dragoe N. 2017. Controlled Jahn-Teller distortion in (MgCoNiCuZn)O-based high entropy oxides. *J. Alloys Comp.* 704:693–700
14. Pu Y, Zhang Q, Li R, Chen M, Du X, Zhou S. 2019. Dielectric properties and electrocaloric effect of high-entropy $(Na_{0.2}Bi_{0.2}Ba_{0.2}Sr_{0.2}Ca_{0.2})TiO_3$ ceramic. *Appl. Phys. Lett.* 115:223901
15. Liu Y, Jia D, Zhou Y, Zhou Y, Zhao J, et al. 2020. $Zn_{0.1}Ca_{0.1}Sr_{0.4}Ba_{0.4}ZrO_3$: a non-equimolar multicomponent perovskite with low thermal conductivity. *J. Eur. Ceram. Soc.* 40:6272–77
16. Qin Y, Liu J-X, Li F, Wei X, Wu H, Zhang G-J. 2019. A high entropy silicide by reactive spark plasma sintering. *J. Adv. Ceram.* 8:148–52
17. Miracle DB, Senkov ON. 2017. A critical review of high entropy alloys and related concepts. *Acta Mater.* 122:448–511
18. Oses C, Toher C, Curtarolo S. 2020. High-entropy ceramics. *Nat. Rev. Mater.* 5:295–309
19. Zhang RZ, Reece MJ. 2019. Review of high entropy ceramics: design, synthesis, structure and properties. *J. Mater. Chem. A* 7:22148–62
20. Gurao NP, Biswas K. 2020. High-entropy materials: critical review and way forward. *Curr. Sci.* 118:1520–39
21. Berardan D, Franger S, Dragoe D, Meena AK, Dragoe N. 2016. Colossal dielectric constant in high entropy oxides. *Phys. Status Solidi Rapid Res. Lett.* 10:328–33
22. Berardan D, Franger S, Meena AK, Dragoe N. 2016. Room temperature lithium superionic conductivity in high entropy oxides. *J. Mater. Chem. A* 4:9536–41
23. Gild J, Zhang YY, Harrington TJ, Jiang SC, Hu T, et al. 2016. High-entropy metal diborides: a new class of high-entropy materials and a new type of ultrahigh temperature ceramics. *Sci. Rep.* 6:37946
24. Ye B, Wen T, Nguyen MC, Hao L, Wang C-Z, Chu Y. 2019. First-principles study, fabrication and characterization of $(Zr_{0.25}Nb_{0.25}Ti_{0.25}V_{0.25})C$ high-entropy ceramics. *Acta Mater.* 170:15–23
25. Jiang S, Shao L, Fan T-W, Duan J-M, Chen X-T, Tang B-Y. 2020. Elastic and thermodynamic properties of high entropy carbide (HfTaZrTi)C and (HfTaZrNb)C from ab initio investigation. *Ceram. Int.* 46:15104–12

26. Zhang Q, Zhang J, Li N, Chen W. 2019. Understanding the electronic structure, mechanical properties, and thermodynamic stability of (TiZrHfNbTa)C combined experiments and first-principles simulation. *J. Appl. Phys.* 126:025101
27. Sarker P, Harrington T, Toher C, Oses C, Samiee M, et al. 2018. High-entropy high-hardness metal carbides discovered by entropy descriptors. *Nat. Commun.* 9:4980
28. Kaufmann K, Maryanovsky D, Mellor WM, Zhu C, Rosengarten AS, et al. 2020. Discovery of high-entropy ceramics via machine learning. *NPJ Comput. Mater.* 6:42
29. Toher C, Oses C, Hicks D, Curtarolo S. 2019. Unavoidable disorder and entropy in multi-component systems. *NPJ Comput. Mater.* 5:69
30. Friedrich R, Usanmaz D, Oses C, Supka A, Fornari M, et al. 2019. Coordination corrected ab initio formation enthalpies. *NPJ Comput. Mater.* 5:59
31. Lu H, Zhao C, Wang H, Liu X, Yu R, Song X. 2019. Hardening tungsten carbide by alloying elements with high work function. *Acta Crystallogr. Sect. B* 75:994–1002
32. Kundu A, Ma J, Carrete J, Madsen GKH, Li W. 2020. Anomalously large lattice thermal conductivity in metallic tungsten carbide and its origin in the electronic structure. *Mater. Today Phys.* 13:100214
33. Holleck H. 1986. Material selection for hard coatings. *J. Vac. Sci. Technol. A* 4:2661–69
34. Jhi SH, Ihm J, Loule SG, Cohen ML. 1999. Electronic mechanism of hardness enhancement in transition-metal carbonitrides. *Nature* 399:132–34
35. Balasubramanian K, Khare SV, Gall D. 2018. Valence electron concentration as an indicator for mechanical properties in rocksalt structure nitrides, carbides and carbonitrides. *Acta Mater.* 152:175–85
36. Harrington TJ, Gild J, Sarker P, Toher C, Rost CM, et al. 2019. Phase stability and mechanical properties of novel high entropy transition metal carbides. *Acta Mater.* 166:271–80
37. Lim M. 2020. *Understanding the thermal, structural, and electrical properties of high entropy oxides and carbides, using computational modeling*. PhD Diss., N.C. State Univ., Raleigh, NC
38. Chen XQ, Fu CL, Krčmar M, Painter GS. 2008. Electronic and structural origin of ultraincompressibility of 5d transition-metal diborides MB_2 (M = W, Re, Os). *Phys. Rev. Lett.* 100:196403
39. Wang N, Fu Z, Legut D, Wei B, Germann TC, Zhang R. 2019. Designing ultrastrong 5d transition metal diborides with excellent stability for harsh service environments. *Phys. Chem. Chem. Phys.* 21:16095–107
40. Braun JL, Rost CM, Lim M, Giri A, Olson DH, et al. 2018. Charge induced disorder controls the thermal conductivity of entropy stabilized oxides. *Adv. Mater.* 30:1805004
41. Lim M, Rak Z, Braun JL, Rost CM, Kotsonis GN, et al. 2019. Influence of mass and charge disorder on the phonon thermal conductivity of entropy stabilized oxides determined by molecular dynamics simulations. *J. Appl. Phys.* 125:055105
42. Rak Z, Rost CM, Lim M, Sarker P, Toher C, et al. 2016. Charge compensation and electrostatic transferability in three entropy-stabilized oxides: results from density functional theory calculations. *J. Appl. Phys.* 120:095105
43. Dai FZ, Wen B, Sun Y, Xiang H, Zhou Y. 2020. Theoretical prediction on thermal and mechanical properties of high entropy $(Zr_{0.2}Hf_{0.2}Ti_{0.2}Nb_{0.2}Ta_{0.2})C$ by deep learning potential. *J. Mater. Sci. Technol.* 43:168–74
44. Rost CM, Borman T, Hossain MD, Lim M, Quiambo-Tomko KF, et al. 2020. Electron and phonon thermal conductivity in high entropy carbides with variable carbon content. *Acta Mater.* 196:231–39
45. Feng L, Lee SH, Kim HN. 2017. Effects of high-energy ball milling and reactive spark plasma sintering on the densification of HfC-SiC composites. *J. Eur. Ceram. Soc.* 37:1891–98
46. Zhang Y, Guo WM, Jiang ZB, Zhu QQ, Sun SK, et al. 2019. Dense high-entropy boride ceramics with ultra-high hardness. *Scr. Mater.* 164:135–39
47. Liu D, Wen TQ, Ye BL, Chu YH. 2019. Synthesis of superfine high-entropy metal diboride powders. *Scr. Mater.* 167:110–14
48. Wen TQ, Ning SS, Liu D, Ye BL, Liu HH, Chu YH. 2019. Synthesis and characterization of the ternary metal diboride solid-solution nanopowders. *J. Am. Ceram. Soc.* 102:4956–62
49. Monteverde F, Saraga F. 2020. Entropy stabilized single-phase (Hf,Nb,Ta,Ti,Zr)B_2 solid solution powders obtained via carbo/boro-thermal reduction. *J. Alloys Compd.* 824:153930
50. Shen XQ, Liu JX, Li F, Zhang GJ. 2019. Preparation and characterization of diboride-based high entropy $(Ti_{0.2}Zr_{0.2}Hf_{0.2}Nb_{0.2}Ta_{0.2})B_2$-SiC particulate composites. *Ceram. Int.* 45(18):24508–14

51. Gild J, Wright A, Quiambao-Tomko K, Qin M, Tomko JA, et al. 2020. Thermal conductivity and hardness of three single-phase high-entropy metal diborides fabricated by borocarbothermal reduction and spark plasma sintering. *Ceram. Int.* 46:6906–13
52. Gu JF, Zou J, Sun SK, Wang H, Yu SY, et al. 2019. Dense and pure high-entropy metal diboride ceramics sintered from self-synthesized powders via boro/carbothermal reduction approach. *Sci. China Mater.* 62:1898–909
53. Feng L, Fahrenholtz WG, Hilmas GE. 2020. Two-step synthesis process for high-entropy diboride powders. *J. Am. Ceram. Soc.* 103(2):724–30
54. Tallarita G, Licheri R, Garroni S, Orru R, Cao G. 2019. Novel processing route for the fabrication of bulk high-entropy metal diborides. *Scr. Mater.* 158:100–4
55. Tallarita G, Licheri R, Garroni S, Barbarossa S, Orru R, Cao G. 2020. High-entropy transition metal diborides by reactive and non-reactive spark plasma sintering: a comparative investigation. *J. Eur. Ceram. Soc.* 40:942–52
56. Failla S, Galizia P, Fu S, Grasso S, Sciti D. 2020. Formation of high entropy metal diborides using arc-melting and combinatorial approach to study quinary and quaternary solid solutions. *J. Eur. Ceram. Soc.* 40:588–93
57. Baik S, Becher PF. 1987. Effect of oxygen contamination on densification of TiB_2. *J. Am. Ceram. Soc.* 70(8):527–30
58. Fahrenholtz WG, Hilmas GE, Zhang SC, Zhu S. 2008. Pressureless sintering of zirconium diboride: particle size and additive effects. *J. Am. Ceram. Soc.* 91(5):1398–404
59. Sciti D, Guicciardi S, Nygren M. 2008. Densification and mechanical behavior of HfC and HfB_2 fabricated by spark plasma sintering. *J. Am. Ceram. Soc.* 91(5):1433–40
60. Wang HL, Lee SL, Feng L. 2014. The processing and properties of (Zr, Hf)B_2–SiC nanostructured composites. *J. Eur. Ceram. Soc.* 34(15):4105–9
61. Zamora V, Ortiz AL, Guiberteau F, Nygren M. 2012. Crystal-size dependence of the spark-plasma-sintering kinetics of ZrB_2 ultra-high-temperature ceramics. *J. Eur. Ceram. Soc.* 32(2):271–76
62. Zhang Y, Jiang ZB, Sun SK, Guo WM, Chen QS, et al. 2019. Microstructure and mechanical properties of high-entropy borides derived from boro/carbothermal reduction. *J. Eur. Ceram. Soc.* 39:3920–24
63. Feng L, Fahrenholtz WG, Hilmas GE. 2020. Processing of dense high-entropy boride ceramics. *J. Eur. Ceram. Soc.* 40(12):3815–23
64. Cologna M, Rashkova B, Raj R. 2010. Flash sintering of nanograin zirconia in <5 s at 850°C. *J. Am. Ceram. Soc.* 93(11):3556–59
65. Yu M, Grasso S, Mckinnon R, Saunders T, Reece MJ. 2017. Review of flash sintering: materials, mechanisms and modelling. *Adv. Appl. Ceram.* 116(1):24–60
66. Gild J, Kaufmann K, Vecchio KS, Luo J. 2019. Reactive flash spark plasma sintering of high-entropy ultrahigh temperature ceramics. *Scr. Mater.* 170:106–10
67. Chen H, Xiang HM, Dai FZ, Liu JC, Zhou YC. 2019. Porous high entropy $(Zr_{0.2}Hf_{0.2}Ti_{0.2}Nb_{0.2}Ta_{0.2})B_2$: a novel strategy towards making ultrahigh temperature ceramics thermal insulating. *J. Mater. Sci. Technol.* 35:2404–8
68. Feng L, Fahrenholtz WG, Hilmas GE, Monteverde F. 2021. Effect of Nb content on the phase composition, densification, microstructure, and mechanical properties of high-entropy boride ceramics. *J. Eur. Ceram. Soc.* 41:92–100
69. Monteverde F, Saraga F, Gaboardi M. 2020. Compositional disorder and sintering of entropy stabilized (Hf,Nb,Ta,Ti,Zr)B_2 solid solution powders. *J. Eur. Ceram. Soc.* 40:3807–14
70. Zhang Y, Sun SK, Zhang W, You Y, Guo WM, et al. 2020. Improved densification and hardness of high-entropy diboride ceramics from fine powders synthesized via borothermal reduction process. *Ceram. Int.* 46:14299–303
71. Ye YF, Wang Q, Lu J, Liu CT, Yang Y. 2016. High-entropy alloy: challenges and prospects. *Mater. Today* 19:349–62
72. Senkov ON, Senkova SV, Woodward C, Miracle DB. 2013. Low-density, refractory multi-principal element alloys of the Cr-Nb-Ti-V-Zr system: microstructure and phase analysis. *Acta Mater.* 61:1545–57
73. Chen XQ, Niu H, Li D, Li Y. 2011. Modeling hardness of polycrystalline materials and bulk metallic glasses. *Intermetallics* 19:1275–81

74. Teter DM. 1998. Computational alchemy: the search for new superhard materials. *MRS Bull.* 23:22–27
75. Tian Y, Xu B, Zhao Z. 2012. Microscopic theory of hardness and design of novel superhard crystals. *Int. J. Refract. Met. Hard Mater.* 33:93–106
76. Shaffer PTB, Jun CK. 1972. The elastic modulus of dense polycrystalline silicon carbide. *Mater. Res. Bull.* 7:63–69
77. Wang YP, Gan GY, Wang W, Yang Y, Tang BY. 2018. Ab initio prediction of mechanical and electronic properties of ultrahigh temperature high-entropy ceramics $(Hf_{0.2}Zr_{0.2}Ta_{0.2}M_{0.2}Ti_{0.2})B_2$ (M = Nb, Mo, Cr). *Phys. Status Solidi B* 255:1800011
78. Backman L, Gild J, Luo J, Opila EJ. 2020. Part I: theoretical predictions of preferential oxidation in refractory high entropy materials. *Acta Mater.* 197:20–27
79. Backman L, Gild J, Luo J, Opila EJ. 2020. Part II: experimental verification of computationally predicted preferential oxidation in refractory high entropy ultra-high temperature ceramics. *Acta Mater.* 197:81–90
80. Zhou JY, Zhang JY, Zhang F, Niu B, Lei LW, Wang WM. 2018. High-entropy carbide: a novel class of multicomponent ceramics. *Ceram. Int.* 44(17):22014–18
81. Chicardi E, Garcia-Garrido C, Gotor FJ. 2019. Low temperature synthesis of an equiatomic $(TiZrHfVNb)C_5$ high entropy carbide by a mechanically-induced carbon diffusion route. *Ceram. Int.* 45(17):21858–63
82. Feng L, Fahrenholtz WG, Hilmas GE, Zhou Y. 2019. Synthesis of single-phase high-entropy carbide powders. *Scr. Mater.* 162:90–93
83. Li F, Lu Y, Wang XG, Bao WC, Liu JX, et al. 2019. Liquid precursor-derived high-entropy carbide nanopowders. *Ceram. Int.* 45:22437–41
84. Castle EG, Csanadi T, Grasso S, Dusza J, Reece M. 2018. Processing and properties of high-entropy ultra-high temperature carbides. *Sci. Rep.* 8:8609–20
85. Ye BL, Wen TQ, Huang KH, Wang CZ, Chu YH. 2019. First-principles study, fabrication, and characterization of $(Hf_{0.2}Zr_{0.2}Ta_{0.2}Nb_{0.2}Ti_{0.2})C$ high-entropy ceramic. *J. Am. Ceram. Soc.* 102:4344–52
86. Chen H, Xiang HM, Dai FZ, Liu JC, Lei YM, et al. 2019. High porosity and low thermal conductivity high entropy $(Zr_{0.2}Hf_{0.2}Ti_{0.2}Nb_{0.2}Ta_{0.2})C$. *J. Mater. Sci. Technol.* 35:1700–5
87. Wei XF, Liu JX, Li F, Qin Y, Liang YC, Zhang GJ. 2019. High entropy carbide ceramics from different starting materials. *J. Eur. Ceram. Soc.* 39:2989–94
88. Wang K, Chen L, Xu CG, Zhang W, Liu ZG, et al. 2019. Microstructure and mechanical properties of (TiZrNbTaMo)C high-entropy ceramic. *J. Mater. Sci. Technol.* 39:99–105
89. Wei XF, Qin Y, Liu JX, Li F, Liang YC, Zhang GJ. 2020. Gradient microstructure development and grain growth inhibition in high-entropy carbide ceramics prepared by reactive spark plasma sintering. *J. Eur. Ceram. Soc.* 40:935–41
90. Feng L, Fahrenholtz WG, Hilmas GE. 2019. Low-temperature sintering of single-phase, high-entropy carbide ceramics. *J. Am. Ceram. Soc.* 102:7217–24
91. Smith CJ, Yu XX, Guo QY, Weinberger CR, Thompson GB. 2018. Phase, hardness, and deformation slip behavior in mixed $Hf_xTa_{1-x}C$. *Acta Mater.* 145:142–53
92. Wang F, Zhang X, Yan XL, Lu YF, Nastasi M, et al. 2020. The effect of submicron grain size on thermal stability and mechanical properties of high-entropy carbides ceramics. *J. Am. Ceram. Soc.* 103:4463–72
93. Feng L, Chen WT, Fahrenholtz WG, Hilmas GE. 2020. Strength of single-phase high-entropy carbide ceramics up to 2300°C. *J. Am. Ceram. Soc.* 104:419–27
94. Ye BL, Wen TQ, Liu D, Chu YH. 2019. Oxidation behavior of $(Hf_{0.2}Zr_{0.2}Ta_{0.2}Nb_{0.2}Ti_{0.2})C$ high-entropy ceramics at 1073–1473 K in air. *Corros. Sci.* 153:327–32
95. Ye BL, Wen TQ, Chu YH. 2020. High-temperature oxidation behavior of $(Hf_{0.2}Zr_{0.2}Ta_{0.2}Nb_{0.2}Ti_{0.2})C$ high-entropy ceramics in air. *J. Am. Ceram. Soc.* 103:500–7
96. Tan YQ, Chen C, Li SQ, Han XC, Xue JX, et al. 2020. Oxidation behaviors of high-entropy transition metal carbides in 1200°C water vapor. *J. Alloys Comp.* 816:152523
97. Wang HX, Cao YJ, Liu W, Wang YG. 2020. Oxidation behavior of $(Hf_{0.2}Ta_{0.2}Zr_{0.2}Ti_{0.2}Nb_{0.2})C$-xSiC ceramics at high temperature. *Ceram. Int.* 46:11160–68

Annual Review of Materials Research

Volume 51, 2021

Contents

Mixed Transport Polymers

Structural Materials

Current Interest

Indexes

Errata

An online log of corrections to *Annual Review of Materials Research* articles may be found at http://www.annualreviews.org/errata/matsci